PHYSICAL REVIEW LETTERS **131,** 041003 (2023)

Editors' Suggestion **Featured in Physics**

First Dark Matter Search with Nuclear Recoils from the XENONnT Experiment

E. Aprile,[1] K. Abe,[2] F. Agostini,[3] S. Ahmed Maouloud,[4] L. Althueser,[5,*] B. Andrieu,[4] E. Angelino,[6] J. R. Angevaare,[7] V. C. Antochi,[8] D. Antón Martin,[9] F. Arneodo,[10] L. Baudis,[11] A. L. Baxter,[12] M. Bazyk,[13] L. Bellagamba,[3] R. Biondi,[14] A. Bismark,[11] E. J. Brookes,[7] A. Brown,[15] S. Bruenner,[7] G. Bruno,[13] R. Budnik,[16] T. K. Bui,[2] C. Cai,[17] J. M. R. Cardoso,[18] D. Cichon,[14] A. P. Cimental Chavez,[11] A. P. Colijn,[7] J. Conrad,[8] J. J. Cuenca-García,[11] J. P. Cussonneau,[13,†] V. D'Andrea,[19,‡] M. P. Decowski,[7] P. Di Gangi,[3] S. Di Pede,[7] S. Diglio,[13] K. Eitel,[20] A. Elykov,[20] S. Farrell,[21] A. D. Ferella,[22,19] C. Ferrari,[19] H. Fischer,[15] M. Flierman,[7] W. Fulgione,[6,19] C. Fuselli,[7] P. Gaemers,[7] R. Gaior,[4] A. Gallo Rosso,[8] M. Galloway,[11] F. Gao,[17] R. Glade-Beucke,[15] L. Grandi,[9] J. Grigat,[15] H. Guan,[12] M. Guida,[14] R. Hammann,[14] A. Higuera,[21] C. Hils,[23] L. Hoetzsch,[14] N. F. Hood,[24] J. Howlett,[1] M. Iacovacci,[25] Y. Itow,[26] J. Jakob,[5] F. Joerg,[14] A. Joy,[8] N. Kato,[2] M. Kara,[20] P. Kavrigin,[16] S. Kazama,[26] M. Kobayashi,[26] G. Koltman,[16] A. Kopec,[24] F. Kuger,[15] H. Landsman,[16] R. F. Lang,[12] L. Levinson,[16] I. Li,[21] S. Li,[12] S. Liang,[21] S. Lindemann,[15] M. Lindner,[14] K. Liu,[17] J. Loizeau,[13] F. Lombardi,[23] J. Long,[9] J. A. M. Lopes,[18,§] Y. Ma,[24] C. Macolino,[22,19] J. Mahlstedt,[8] A. Mancuso,[3] L. Manenti,[10] F. Marignetti,[25] T. Marrodán Undagoitia,[14] K. Martens,[2] J. Masbou,[13] D. Masson,[15] E. Masson,[4] S. Mastroianni,[25] M. Messina,[19] K. Miuchi,[27] K. Mizukoshi,[27] A. Molinario,[6] S. Moriyama,[2] K. Morå,[1,∥] Y. Mosbacher,[16] M. Murra,[1] J. Müller,[15] K. Ni,[24] U. Oberlack,[23] B. Paetsch,[16] J. Palacio,[14] R. Peres,[11] C. Peters,[21] J. Pienaar,[9] M. Pierre,[7,13] V. Pizzella,[14] G. Plante,[1] J. Qi,[24] J. Qin,[12] D. Ramírez García,[11] R. Singh,[12] L. Sanchez,[21] J. M. F. dos Santos,[18] I. Sarnoff,[10] G. Sartorelli,[3] J. Schreiner,[14] D. Schulte,[5] P. Schulte,[5] H. Schulze Eißing,[5] M. Schumann,[15] L. Scotto Lavina,[4] M. Selvi,[3] F. Semeria,[3] P. Shagin,[23] S. Shi,[1] E. Shockley,[24] M. Silva,[18] H. Simgen,[14] A. Takeda,[2] P.-L. Tan,[8] A. Terliuk,[14,¶] D. Thers,[13] F. Toschi,[20,15] G. Trinchero,[6] C. Tunnell,[21] F. Tönnies,[15] K. Valerius,[20] G. Volta,[11] C. Weinheimer,[5] M. Weiss,[16] D. Wenz,[23,**] C. Wittweg,[11] T. Wolf,[14] V. H. S. Wu,[20] Y. Xing,[13] D. Xu,[1] Z. Xu,[1] M. Yamashita,[2] L. Yang,[24] J. Ye,[1] L. Yuan,[9] G. Zavattini,[28] M. Zhong,[24] and T. Zhu[1]

(XENON Collaboration)[††]

[1]*Physics Department, Columbia University, New York, New York 10027, USA*
[2]*Kamioka Observatory, Institute for Cosmic Ray Research, and Kavli Institute for the Physics and Mathematics of the Universe (WPI), University of Tokyo, Higashi-Mozumi, Kamioka, Hida, Gifu 506-1205, Japan*
[3]*Department of Physics and Astronomy, University of Bologna and INFN-Bologna, 40126 Bologna, Italy*
[4]*LPNHE, Sorbonne Université, CNRS/IN2P3, 75005 Paris, France*
[5]*Institut für Kernphysik, Westfälische Wilhelms-Universität Münster, 48149 Münster, Germany*
[6]*INAF-Astrophysical Observatory of Torino, Department of Physics, University of Torino and INFN-Torino, 10125 Torino, Italy*
[7]*Nikhef and the University of Amsterdam, Science Park, 1098XG Amsterdam, Netherlands*
[8]*Oskar Klein Centre, Department of Physics, Stockholm University, AlbaNova, Stockholm SE-10691, Sweden*
[9]*Department of Physics and Kavli Institute for Cosmological Physics, University of Chicago, Chicago, Illinois 60637, USA*
[10]*New York University Abu Dhabi—Center for Astro, Particle and Planetary Physics, Abu Dhabi, United Arab Emirates*
[11]*Physik-Institut, University of Zürich, 8057 Zürich, Switzerland*
[12]*Department of Physics and Astronomy, Purdue University, West Lafayette, Indiana 47907, USA*
[13]*SUBATECH, IMT Atlantique, CNRS/IN2P3, Université de Nantes, Nantes 44307, France*
[14]*Max-Planck-Institut für Kernphysik, 69117 Heidelberg, Germany*
[15]*Physikalisches Institut, Universität Freiburg, 79104 Freiburg, Germany*
[16]*Department of Particle Physics and Astrophysics, Weizmann Institute of Science, Rehovot 7610001, Israel*
[17]*Department of Physics & Center for High Energy Physics, Tsinghua University, Beijing 100084, China*
[18]*LIBPhys, Department of Physics, University of Coimbra, 3004-516 Coimbra, Portugal*
[19]*INFN-Laboratori Nazionali del Gran Sasso and Gran Sasso Science Institute, 67100 L'Aquila, Italy*
[20]*Institute for Astroparticle Physics, Karlsruhe Institute of Technology, 76021 Karlsruhe, Germany*
[21]*Department of Physics and Astronomy, Rice University, Houston, Texas 77005, USA*
[22]*Department of Physics and Chemistry, University of L'Aquila, 67100 L'Aquila, Italy*
[23]*Institut für Physik and Exzellenzcluster PRISMA$^+$, Johannes Gutenberg-Universität Mainz, 55099 Mainz, Germany*
[24]*Department of Physics, University of California San Diego, La Jolla, California 92093, USA*
[25]*Department of Physics "Ettore Pancini," University of Napoli and INFN-Napoli, 80126 Napoli, Italy*
[26]*Kobayashi-Maskawa Institute for the Origin of Particles and the Universe, and Institute for Space-Earth Environmental Research, Nagoya University, Furo-cho, Chikusa-ku, Nagoya, Aichi 464-8602, Japan*
[27]*Department of Physics, Kobe University, Kobe, Hyogo 657-8501, Japan*
[28]*INFN—Ferrara and Dip. di Fisica e Scienze della Terra, Università di Ferrara, 44122 Ferrara, Italy*

0031-9007/23/131(4)/041003(9) Published by the American Physical Society

(Received 6 March 2023; accepted 22 June 2023; published 28 July 2023)

We report on the first search for nuclear recoils from dark matter in the form of weakly interacting massive particles (WIMPs) with the XENONnT experiment, which is based on a two-phase time projection chamber with a sensitive liquid xenon mass of 5.9 ton. During the (1.09 ± 0.03) ton yr exposure used for this search, the intrinsic ^{85}Kr and ^{222}Rn concentrations in the liquid target are reduced to unprecedentedly low levels, giving an electronic recoil background rate of (15.8 ± 1.3) events/ton yr keV in the region of interest. A blind analysis of nuclear recoil events with energies between 3.3 and 60.5 keV finds no significant excess. This leads to a minimum upper limit on the spin-independent WIMP-nucleon cross section of 2.58×10^{47} cm^2 for a WIMP mass of 28 GeV$/c^2$ at 90% confidence level. Limits for spin-dependent interactions are also provided. Both the limit and the sensitivity for the full range of WIMP masses analyzed here improve on previous results obtained with the XENON1T experiment for the same exposure.

DOI: 10.1103/PhysRevLett.131.041003

Astrophysical and cosmological observations indicate the existence of a massive, nonluminous, nonrelativistic, and nonbaryonic dark matter (DM) component of the Universe [1]. One well-motivated class of DM candidates is weakly interacting massive particles (WIMPs), which arise naturally in several beyond-standard-model theories [2]. Direct detection searches for WIMPs with masses of a few GeV$/c^2$ to tens of TeV$/c^2$ using liquid xenon (LXe) time projection chambers (TPCs) have produced the most stringent limits to date on elastic spin-independent WIMP-nucleon cross sections [3–5].

The XENON Dark Matter project currently operates the XENONnT experiment at the INFN Laboratori Nazionali del Gran Sasso (LNGS) underground laboratory. It is an upgrade of its predecessor, XENON1T [6], with a new, larger dual-phase TPC featuring a sensitive LXe mass of 5.9 ton. The XENON1T cryogenics, gaseous purification, and krypton distillation systems, as well as the 700 ton water Cherenkov muon veto (MV) tank [7,8] are reused to operate XENONnT. Inside the water tank, a new neutron veto (NV) detector encloses the TPC cryostat. For the exposure used in this analysis, the NV was operated as a water Cherenkov detector, tagging neutrons through their capture on hydrogen which releases a 2.22 MeV γ ray.

The sensitive LXe detector volume enclosed by a polytetrafluoroethylene (PTFE) cylinder with a height of 1.49 m and a diameter of 1.33 m is viewed by 494 Hamamatsu R11410-21 3 in. photomultiplier tubes (PMTs) [9] distributed in a top and a bottom array. To fill the vessel housing the TPC a total of 8.5 ton liquified xenon is required which is continuously purified by a new liquid-phase purification system [10]. Together with a high flow radon distillation system [11], a careful selection of detector construction materials [12], and a specialized assembly procedure, this led to an unprecedentedly low electronic recoil (ER) background of (15.8 ± 1.3) events/ton yr keV below recoil energies of 30 keV [13].

Particles depositing energy in the LXe produce a prompt scintillation signal (S1) as well as ionization electrons which drift upward and are extracted into the gas above the liquid due to applied electric fields. Here a second scintillation signal (S2) proportional to the number of extracted electrons is produced. WIMPs are expected to primarily produce nuclear recoils (NRs), where a xenon nucleus recoils, while the background is dominated by ER interactions where an electron recoils. A higher scintillation-to-ionization ratio is expected for NRs, but unlike ERs, a fraction of the total recoil energy is also lost as unobservable heat.

Three parallel-wire electrodes (cathode, gate, and anode) are used to establish the drift and extraction fields. The gate and anode electrodes are reinforced with two and four transverse wires, respectively, to minimize wire sagging. Two additional parallel-wire screening electrodes are used to shield the PMT arrays from the electric fields. After two months of commissioning at a drift field of 100 V/cm, a short between the bottom screening and cathode electrodes limited the applied drift field to 23 V/cm, corresponding to a maximum drift time of 2.2 ms. The extraction field was set to 2.9 kV/cm in LXe to reduce localized, intermittent bursts of single electron S2 signals. Despite the lower-than-designed drift and extraction fields, the energy and position resolution, as well as the energy threshold, are comparable to those achieved with XENON1T.

The TPC and veto detectors are integrated into a single data acquisition system [14]. The data acquired by the MV uses the same hardware event trigger as in XENON1T [15], whereas data from the TPC and NV are acquired in a "triggerless" mode, with each individual PMT channel recording all signals above a channel-specific threshold of 0.13 photoelectrons (PE).

The recorded signals are processed using custom-developed open source software packages [16,17]. Each PMT signal is scanned for PMT "hits" above threshold, and hits found in the TPC channels are clustered and classified into S1, S2, or "unclassified" peaks based on pulse shape and PMT hit pattern. At least three PMTs must contribute to an S1 within ±50 ns around the center of the integrated peak waveform. Events are built in time intervals between 2.45 ms before and 0.25 ms after S2s, and overlapping events are merged. The event S2 is required to be greater than 100 PE, and have fewer than eight other peaks larger than half of the S2 peak area within ±10 ms.

The PMT hit patterns of S2 signals are used to reconstruct the horizontal position (X, Y) of an event using neural network models [18,19]. Each model was trained by the S2 light distribution on the top PMT array generated through optical simulations with GEANT4 [8] corrected for the number of excluded PMTs and electronics per-PMT response with the XENONnT waveform simulator (WFSim) [20]. The horizontal interaction position resolution for simulated events close to the PTFE detector walls is 1 cm, and 0.75 cm within the fiducial volume (FV), for a 1000 PE S2 (30 extracted electrons). The depth Z of an interaction is reconstructed from the measured drift time between S1 and S2 and the electron drift velocity with a resolution $< 1\%$. The 50% S2 width of a single electron signal is about 600 ns, and the width of S2s within the FV of the detector typically range from 2 to 9 μs. The drift field has a radial component that shifts ionization electrons originating deeper in the detector inward when they are observed at the liquid surface. This inward shift is corrected with a data-driven approach, assuming a uniform distribution of $^{83\mathrm{m}}$Kr calibration events in radius squared (R^2) as in Ref. [18].

The position and time information of the detected S1 and S2 signals is used to correct for the inhomogeneous detector response due to quanta generation and collection effects, and corresponds to corrections of up to 30% for either signals. Scintillation photons are affected by a position-dependent optical light collection efficiency which reduces the S1 peak area. A light yield (LY) map normalized to the mean response in the FV is generated using $^{83\mathrm{m}}$Kr signals. The electric field dependence of the LY is removed using a drift field map constructed by matching the spatial distribution of $^{83\mathrm{m}}$Kr to a COMSOL [21] simulation, accounting for potential charge accumulations on the PTFE surfaces. This drift field map was validated with data using the measured S1 ratio of the two $^{83\mathrm{m}}$Kr decays [22]. The resulting LY map is valid over the full energy range of this analysis and is used to correct S1 signals referred to as cS1.

The S2 peak area reduces exponentially for signals deeper in the detector, as drifting electrons can be captured by electronegative impurities. This effect leads to a time-dependent lifetime of the free electrons which is corrected using data from $^{83\mathrm{m}}$Kr and ^{222}Rn decays, and monitored with a new purity monitor system [23]. The charge yield of the respective sources was corrected by the drift field map using low-field data from Ref. [24]. An electron lifetime better than 10 ms was reached throughout the science run with a liquid purification flow of 8.3 ton/d [10]. The spatial variation in the S2 response is dominated by the position-dependent optical light collection efficiency and inhomogeneous electroluminescence amplification. $^{83\mathrm{m}}$Kr events are used to obtain a normalized horizontal S2 peak area correction map. Time-dependent variations of the single electron gain and extraction efficiency following each ramping up of the electric field are corrected by their respective data-driven trends. S2 signals summed over the top and bottom array and corrected for the above effects are referred to as cS2.

The method to convert the cS1 and cS2 signals of NRs and ERs into a combined energy scale is described in Ref. [25]. The photon and electron gains are found to be $g_1 = (0.151 \pm 0.001)$ PE/photon and $g_2 = (16.5 \pm 0.6)$ PE/electron, assuming the mean energy to produce a charge or light quantum to 13.7 eV/quantum [26]. Reconstructed energies using this scale directly give the ER-equivalent energy ($\mathrm{keV_{ER}}$), while the NR-equivalent energy ($\mathrm{keV_{NR}}$) requires a model for energy lost to heat, and uses the full NR detector model described later.

The science search data were collected from July 6 to November 10, 2021. This period named Science Run 0 (SR0) contains a total of 97.1 d of data which correspond to a dead-time- and veto-corrected live time of 95.1 d. The length of SR0 was primarily chosen to investigate the XENON1T ER excess [25], leading to a WIMP search exposure of (1.09 ± 0.03) ton yr. The detector conditions were stable throughout SR0 with an average LXe temperature of (176.8 ± 0.4) K and pressure of (1.890 ± 0.004) bar, where the uncertainties represent the corresponding rms over SR0. PMT gains were monitored by weekly calibrations with a pulsed low-intensity light source, and voltages were adjusted at the beginning of SR0 to achieve 2×10^6 gains for all PMTs. The time dependence of the PMT gains was modeled and the signals were corrected, resulting in a gain variation $< 3\%$. In total, 17 PMTs were excluded from analysis due to internal vacuum degradation, instability, light emission, or noise. Five of these PMTs are distributed evenly in the top PMT array. Periods of data taken with an intermittent and localized high rate of S2 emission from single or few electrons are not included in calibration and search data. Calibrations with $^{83\mathrm{m}}$Kr were performed every second week to correct the detector response for position- and time-dependent effects, and to monitor the stability of cS1 and cS2.

The NR response of XENONnT and the NV tagging efficiency were calibrated using an external ^{241}AmBe source which was placed in three positions close to the

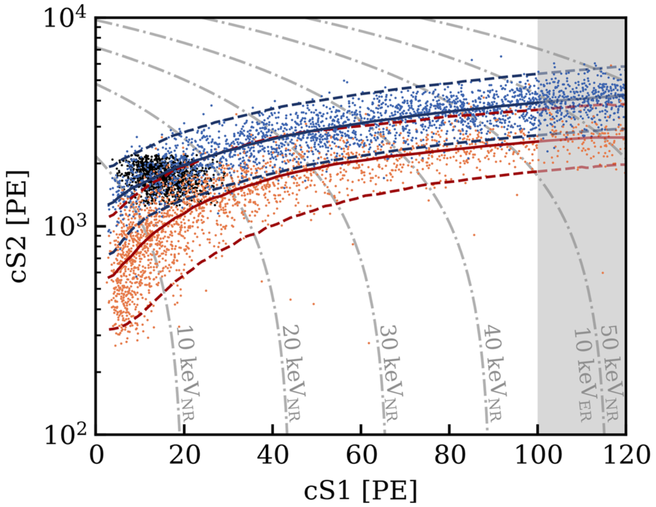

FIG. 1. NR and ER calibration data from ^{241}AmBe (orange), ^{222}Rn (blue), and ^{37}Ar (black). The median and the $\pm 2\sigma$ contours of the NR and ER model are shown in blue and red, respectively. The gray dash-dotted contour lines show the reconstructed NR energy (keV$_{\mathrm{NR}}$). Only not shaded events up to a cS1 of 100 PE are considered in the response model fits.

TPC cryostat. ^{241}AmBe emits neutrons via the alpha-capture reaction $^9\mathrm{Be}(\alpha, n)^{12}\mathrm{C}$, which has a chance of about 60% to emit an additional 4.44 MeV γ ray [27]. This γ ray, well above the NV threshold, is used to select NR S1 signals in a 400 ns window. After applying the same data-quality cuts as used in the main analysis, 1986 events remain in the region of interest (ROI) shown in Fig. 1. Only 1.8 ± 0.6 events are expected from random coincidences between the two detectors, determined through a sideband study. The tagging efficiency of the NV is estimated from the number of delayed neutron capture signals following the NR S1 signals. This data-driven tagging efficiency is corrected for position-dependent effects using GEANT4 [28] simulations which account for the full spatial distribution of neutrons emitted by detector materials [8]. The length of the veto window was set to 250 μs with a fivefold PMT coincidence and a 5 PE event area threshold in the NV. This gives a neutron tagging efficiency of $(53 \pm 3)\%$, and a live time reduction of 1.6%.

The ER response model is calibrated with 2051 ^{212}Pb β events from a ^{222}Rn calibration source [29], before SR0 and with events from an ^{37}Ar source [30] collected after SR0, as discussed in Ref. [13]. NR and ER calibration datasets were fitted using the LXe response model and fast detector simulation described in Ref. [31]. For both datasets, a Markov-chain Monte Carlo sampling of the parameter space gives the best-fit point and posterior distribution. The goodness of fit (GOF) was assessed by partitioning the cS1, cS2 space into equiprobable bins according to both best-fit models and then computing a Poisson χ^2 likelihood, as well as one-dimensional projections on cS2. Neither test rejects the best-fit model, with two-dimensional p-values of 0.18 and 0.39 for ER and NR, respectively, and no significant p-values for the one-dimensional projections. The calibration data and contours of the best-fit model are shown in Fig. 1. The leakage fraction of the ^{220}Rn ER events below the NR median is $1.1^{+0.2}_{-0.3}\%$.

The full ER model has too many parameters to be tractable in the inference toy MC simulations. Using linear combinations of the original parameters identified with a principal component analysis reduces parameter redundancies, and these parameter directions are then ranked according to their impact on the background expectation in a signal-like region in cS1 and cS2. The two parameters with the highest impact are included as nuisance parameters in the ER model used in the WIMP search likelihood.

The ROI is defined by cS1 between 0 and 100 PE and cS2 between 126 and 12 589 PE. Together with detection and selection efficiencies, this gives an energy range with at least 10% total efficiency from 3.3 to 60.5 keV$_{\mathrm{NR}}$. All events reconstructed with an ER energy below 20 keV$_{\mathrm{ER}}$ and found in the cS1 and cS2 contours of the ER and NR band were blinded. For the study of the ER data presented in Ref. [13], all events above the -2σ quantile of the ER band or with a reconstructed ER energy larger than 10 keV$_{\mathrm{ER}}$ were unblinded. The remaining region was unblinded only after finalizing the analysis procedure presented here.

The event selection criteria from Ref. [18] were optimized for the ROI in this analysis. Data quality cuts are applied in order to include only well-reconstructed events and to suppress backgrounds. All cuts were optimized based on calibration data and simulations using WFSim. Each valid event is required to have a valid S1-S2 pair. Events tagged by the MV or NV are removed from the data selection as are multiple-scatter (MS) events since WIMPs are expected to induce only single-scatter (SS) NRs. The MV uses a veto window of 1 ms with a fivefold PMT coincidence and a 10 PE MV event area threshold.

A dedicated cut similar to that in Ref. [32] using a gradient boosted decision tree (GBDT) was developed to reduce the background due to randomly paired S1-S2 signals called accidental coincidences (ACs). This cut uses S2 area and shape, as well as interaction depth, and reduces the AC background by 65% at 95% signal acceptance. Because of an insufficient model of the S2 pulse shape near the transverse wires caused by local variations of the drift and extraction field with respect to the rest of the TPC, an optimization of the GBDT and other S2 shape-based cuts was not possible with WFSim. Consequently, the LXe target is split into two parts in the modeling for the WIMP search. A less strict data-driven model for the S2 width cut and no GBDT selection is used in an 8.9 cm wide band around the transverse wires, leading to a lower signal-to-background ratio, but with a 10% higher selection efficiency. The total selection efficiency for these "near"- and "far-wire" regions is estimated following the procedure in

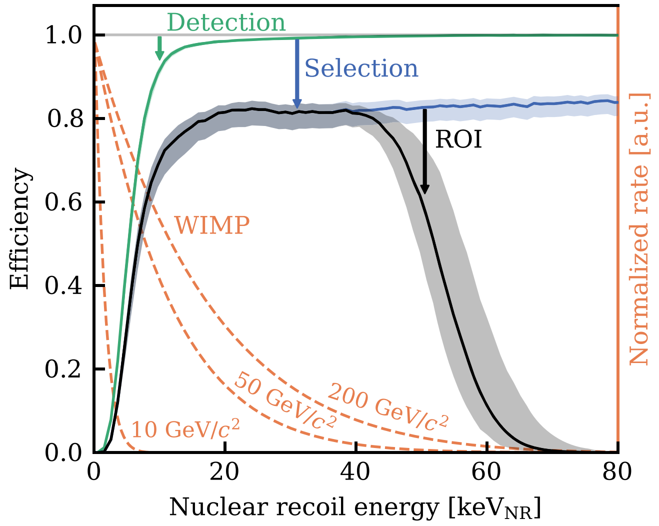

FIG. 2. Detection and selection efficiency for NR events in this search as a function of the NR recoil energy. The total efficiency in the WIMP search region (black) is dominated by the detection efficiency (green) at low energies and event selections (blue) at higher energies until the edge of the ROI. Normalized recoil spectra for WIMPs with masses of 10, 50, and 200 GeV/c^2 are shown with orange dashed lines for reference.

Refs. [18,25]. Efficiency losses due to the event building are also taken into account in the selection efficiency.

The detection efficiency of the TPC dominated by the S1 detection efficiency is evaluated using WFSim and validated with a data-driven method [31,33]. Both methods agree within 1%. Efficiency losses at small energies are dominated by the threefold PMT coincidence requirement. The upper cS1 ROI edge chosen to include the full WIMP spectrum determines the upper edge of this analysis. The combined selection efficiency of the near- and far-wire regions, the detection, and the total efficiencies of the analysis are shown together with the normalized recoil spectra of three different WIMP masses in Fig. 2.

In order to mitigate background events from detector radioactivity as well as "surface events" produced by ERs from ^{210}Pb plate-out [3], only events reconstructed in a central FV (illustrated in the Supplemental Material [34], Fig. S2) are considered in the analysis. The FV shape is optimized based on the background distributions, as well as constrained to not include regions where the detector is not sensitive or models are incomplete. The total LXe mass of the FV after considering the systematic uncertainty of the field distortion correction is (4.18 ± 0.13) ton.

Five different background components make up the total background model: radiogenic neutrons, coherent elastic neutrino-nucleus scattering (CEνNS), ERs, surface events, and ACs. The expectation values for each are summarized in Table I. In addition to the full expectation values, we include for illustration expectation values in a signal-like region defined to contain half of a 200 GeV/c^2 WIMP signal with the lowest signal-to-background ratio.

The NR background in XENONnT is dominated by radiogenic neutrons from spontaneous fission and (α, n) reactions. Neutron yields and energies originating from various detector materials are evaluated as in Refs. [8,31]. A custom interface based on the fitted NR model accepts GEANT4 simulation inputs, and provides observable quanta processed by WFSim to construct the neutron background model [38]. The neutron rate was estimated based on this full detector simulation and compared against a data-driven method. The data-driven estimate uses a combined Poisson likelihood for MS and SS events tagged by the NV, together with a simulation-driven MS:SS ratio which was validated with ^{241}AmBe data. The maximum deviation of the MS:SS ratio estimated as a function of the radius between data and simulation was found to be less than 20%. However, a wrong sign in the NV tagging window discovered only after unblinding of the main data meant that the simulation and data-driven estimates found before were no longer in agreement. This error arose from the premise that the tagging efficiency was determined in a forward coincidence, counting the number NV tags for a given set of NR SS events, while the tagging is done by a backward veto triggered when a NV event satisfies the threshold criteria. In accordance with the analysis plan, the data-driven rate estimate is used. Four events in the WIMP blinding region are tagged by the NV and cut, three of them also fail the SS cut, compatible with the MS:SS ratio from simulations. This gives a total neutron expectation of $1.1^{+0.6}_{-0.5}$ events which is a factor 6 higher than predicted by simulations. Analysis choices such as the NV tagging window and the FV were not reoptimized after this correction.

The remaining contribution to the NR background is predominately due to CEνNS from ^{8}B solar neutrinos. The rate is constrained by measurements of the ^{8}B flux [39], but the total uncertainty of the expectation value is dominated by the detector response model uncertainties. The number of cosmogenic neutrons is conservatively estimated to be fewer than 0.01 events after MV tagging [7], not including the additional suppression by the NV. Thus, this background is considered to be negligible.

The ER background is dominated by β decays of ^{214}Pb originating from the decay of ^{222}Rn in the LXe. Solar neutrino-electron scattering, ^{85}Kr, and γ rays emitted by detector materials also contribute to the ER background [13]. The ER response model fit was updated after unblinding of the main data to use the same data-quality selections as of this study, compared to Ref. [13]. Prior to unblinding, 134 events are found in the ER band of the ROI.

Data-driven models are constructed for AC events and surface background events. The AC background is concentrated at low S1 and S2, and is therefore a particular challenge for low-mass WIMP searches. The model is constructed from a synthetic dataset made from isolated S1s and S2s using the method in Ref. [32]. Looser cuts in

TABLE I. Expected number of events for each model component and observed events. The "nominal" column shows expectation values and uncertainties, if applicable, before unblinding. The nominal ER value is the observed number of ER events before unblinding. Other columns show best-fit expectation values and uncertainties for a free fit including a 200 GeV/c^2 WIMP signal component. The best-fit signal cross section is 3.22×10^{-47} cm^2. In addition to the expectation values in the full ROI, we include the expectation values in a signal-like cS1,cS2 region containing the 50% of signal in with the best signal-to-background ratio. This region is indicated in Fig. 3 with an orange dashed contour. The best-fit and preunblinding values agree within uncertainties for all components which include an ancillary constraint term.

	Nominal	Best fit	
	ROI		Signal-like
ER	134	135^{+12}_{-11}	0.92 ± 0.08
Neutrons	$1.1^{+0.6}_{-0.5}$	1.1 ± 0.4	0.42 ± 0.16
CEνNS	0.23 ± 0.06	0.23 ± 0.06	0.022 ± 0.006
AC	4.3 ± 0.9	$4.4^{+0.9}_{-0.8}$	0.32 ± 0.06
Surface	14 ± 3	12 ± 2	0.35 ± 0.07
Total background	154	152 ± 12	$2.03^{+0.17}_{-0.15}$
WIMP	…	2.6	1.3
Observed	…	152	3

the near-wire region give a 6 times larger AC rate for this region compared to the rest of the TPC. Background sidebands and ^{220}Rn and ^{37}Ar calibration data were used to validate the AC model, and the rate is estimated with an uncertainty of better than 5%. The surface background model is constructed from ^{210}Po events originating from the TPC walls, using a similar method as in Ref. [31]. The data are described in radius using a parametric likelihood fit based on events found below the blinded region. cS1 and cS2 are modeled using a kernel density estimation derived from events reconstructed outside of the TPC. The wall model is validated using the unblinded WIMP region outside of the FV as a sideband. The expected values for both backgrounds are summarized in Table I and their distributions in the (cS1, cS2) space are shown in Fig. 3. An extended table including separate values for the near- and far-wire region is included in the Supplemental Materials [34] as Table S2.

The statistical analysis of the WIMP search data uses toy MC simulations of the experiment to calibrate the distribution of a log-likelihood-ratio test statistic as in Refs. [31,40]. Four terms make up the likelihood: two search-data terms for events near and far from the transverse wires, an ER calibration term, and a term representing ancillary measurements of parameters. The first three are extended unbinned likelihoods in cS1, cS2, as well as R for the first term. All three terms have the same form as Eq. (21) in Ref. [31]. The two search-data likelihoods include components for the ER, AC, surface, CEνNS, and radiogenic neutron backgrounds, as well as the WIMP signal. The ^{220}Rn calibration term includes the ER model as well as an AC component. The expected number of events for each component is a nuisance parameter in the likelihood. In addition, two shape parameters for the ER model are included, and a parameter representing the uncertainty of the expected number of signal events given the NR response model. The ER shape parameters mainly modify the signal-like ER tail below $S1 = 10$ PE, where they allow the signal-like ER tail below the median S2 expected from a 200 GeV/c^2 WIMP to vary between 0.009 and 0.017 at 60% confidence level. The signal shape is fixed, as even a large signal excess would be small enough that the calibration constraints would dominate. The signal expectation value for a certain cross section is included as a nuisance parameter. The ancillary measurement term includes Gaussians representing the measurements constraining the AC, radiogenic, surface, and CEνNS rates, and the uncertain signal expectation.

The signal NR spectrum is modeled with the Helm form factor for the nuclear cross section [41], and a standard halo model with parameters fixed to the recommendations of Ref. [40]. The main change from previous XENON publications is an updated local standard of rest velocity of 238 km/s [42,43]. The NR model fit to

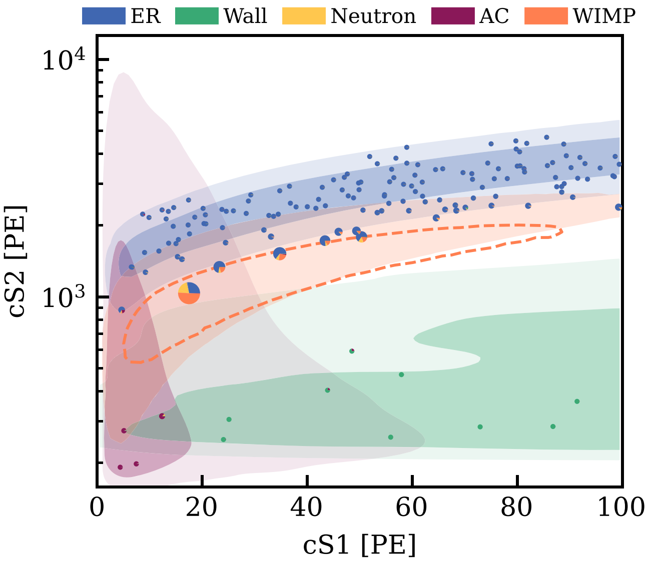

FIG. 3. DM search data in the cS1-cS2 space. Each event is represented with a pie chart showing the fraction of the best-fit model, including the expected number of 200 GeV/c^2 WIMPs (orange) evaluated at the position of the event. The size of the pie charts is proportional to the signal model at that position. Background probability density distributions are shown as 1σ (dark) and 2σ (light) regions as indicated in the legend for ER (blue), AC (purple), and surface (green, "wall"). The neutron background (yellow in pies) has a similar distribution to the WIMP (orange-filled area showing the 2σ region). The orange dashed contour contains a signal-like region which is constructed to contain 50% of a 200 GeV/c^2 WIMP signal with the highest possible signal-to-noise ratio.

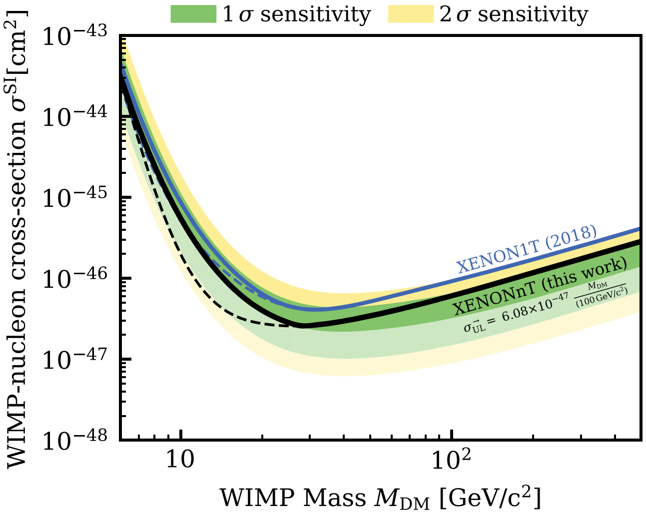

FIG. 4. Upper limit on spin-independent WIMP-nucleon cross section at 90% confidence level (full black line) as a function of the WIMP mass. A power constraint is applied to the limit to restrict it at or above the median unconstrained upper limit. The dashed lines show the upper limit without a power constraint applied. The 1σ (green) and 2σ (yellow) sensitivity bands are shown as shaded regions, with lighter colors indicating the range of possible downward fluctuations. The result from XENON1T [3] is shown in blue with the same power constraint applied. At masses above 100 GeV/c^2, the limit scales with mass as indicated with the extrapolation formula.

calibration data is used to construct a model for the signal in cS1 and cS2.

After unblinding, the ROI contains 152 events, 16 of which were in the blinded WIMP region. The data are shown in Fig. 3, and the best-fit expectation values are in Table I. The binned GOF test indicates no large-scale mismodeling ($p = 0.63$). At high cS1, $\gtrsim$50 PE, we observe more events which are consistent with ER events than our model or calibration data predict, in particular between cS1s of 50 and 75 PE. Of the 16 former blinded events, 13 are found in the upper right half of the horizontal event distribution, with no correlation with the transverse wires observed (see Fig. S3 in Supplemental Material [34]). The ^{220}Rn, $^{83\mathrm{m}}$Kr, and ^{37}Ar calibration datasets do not exhibit any asymmetry, nor is any seen in the acceptances evaluated in the X, Y plane for any of the applied cuts.

The WIMP discovery p-value indicates no significant excess ($p \geq 0.20$, with the minimum for masses above 100 GeV/c^2), and the resulting limits on spin-independent interactions are shown in Fig. 4, with spin-dependent limits included in Figs. S1(a) and S1(b) in Supplemental Material [34]. To constrain large downward fluctuations, the limit is subjected to a power constraint following Ref. [44]. We choose a very conservative power threshold of 50%, higher than that advocated in Ref. [40], as that paper mistakenly defined the power constraint in terms of discovery power when settling on a threshold of 15%. See the Supplemental Material [34] for further discussion. For spin-independent interactions, the lowest upper limit is 2.58×10^{47} cm^2 at 28 GeV/c^2 and 90% confidence level (CL). At masses above 100 GeV/c^2, the limit is 6.08×10^{-47} cm$^2\times$ $(M_{\mathrm{DM}}/(100\ \mathrm{GeV}/c^2))$. For spin-independent interactions, the lowest upper limit is 2.58×10^{47} cm^2 at 28 GeV/c^2 and 90% CL. At masses above 100 GeV/c^2, the limit is 6.08×10^{-47} cm^2 $\times$ $(M_{\mathrm{DM}}/(100\ \mathrm{GeV}/c^2))$.

In conclusion, a blind analysis of 95.1 d of science data with a total exposure of (1.09 ± 0.03) ton yr has been performed. The best fit to the data is compatible with the background-only hypothesis. The experiment has achieved an ER background level of (15.8 ± 1.3) events/ton yr keV, 5 times lower than XENON1T, with comparable detector resolutions, and energy threshold. This results in a sensitivity improvement with respect to XENON1T by a factor of 1.7 at a WIMP mass of 100 GeV/c^2.

Currently, XENONnT continues to take data, with a further reduced ^{222}Rn ER background, using the radon distillation system with combined gaseous and liquid xenon flow. Subsequent data taking is planned with the NV operating as designed, with Gd-sulphate-octahydrate loaded into the water [45,46] to increase the neutron tagging efficiency to 87% with a lower overall lifetime reduction [8].

We gratefully acknowledge support from the National Science Foundation, Swiss National Science Foundation, German Ministry for Education and Research, Max Planck Gesellschaft, Deutsche Forschungsgemeinschaft, Helmholtz Association, Dutch Research Council (NWO), Weizmann Institute of Science, Israeli Science Foundation, Binational Science Foundation, Fundacao para a Ciencia e a Tecnologia, Région des Pays de la Loire, Knut and Alice Wallenberg Foundation, Kavli Foundation, JSPS Kakenhi and JST FOREST Program in Japan, Tsinghua University Initiative Scientific Research Program, and Istituto Nazionale di Fisica Nucleare. This project has received funding or support from the European Union's Horizon 2020 research and innovation program under the Marie Skłodowska-Curie Grant Agreement No. 860881-HIDDeN. Data processing is performed using infrastructures from the Open Science Grid, the European Grid Initiative, and the Dutch national e-infrastructure with the support of SURF Cooperative. We are grateful to Laboratori Nazionali del Gran Sasso for hosting and supporting the XENON project.

---

[*] l.althueser@uni-muenster.de

[†] Deceased.

[‡] Also at INFN—Roma Tre, 00146 Roma, Italy.

[§] Also at Coimbra Polytechnic—ISEC, 3030-199 Coimbra, Portugal.

[∥] knut.dundas.moraa@columbia.edu

[¶] Also at Physikalisches Institut, Universität Heidelberg, Heidelberg, Germany.

[**]dwenz@uni-mainz.de
[††]xenon@lngs.infn.it

[1] G. Bertone, D. Hooper, and J. Silk, Particle dark matter: Evidence, candidates and constraints, Phys. Rep. **405**, 279 (2005).
[2] L. Roszkowski, E. M. Sessolo, and S. Trojanowski, WIMP dark matter candidates and searches—current status and future prospects, Rep. Prog. Phys. **81**, 066201 (2018).
[3] E. Aprile *et al.* (XENON Collaboration), Dark Matter Search Results from a One Ton-Year Exposure of XENON1T, Phys. Rev. Lett. **121**, 111302 (2018).
[4] Y. Meng *et al.* (PandaX Collaboration), Dark Matter Search Results from the PandaX-4T Commissioning Run, Phys. Rev. Lett. **127**, 261802 (2021).
[5] J. Aalbers *et al.* (LZ Collaboration), preceding Letter, First Dark Matter Search Results from the LUX-ZEPLIN (LZ) Experiment, Phys. Rev. Lett. **131**, 041002 (2023).
[6] E. Aprile *et al.* (XENON Collaboration), The XENON1T dark matter experiment, Eur. Phys. J. C **77**, 881 (2017).
[7] E. Aprile *et al.* (XENON Collaboration), Conceptual design and simulation of a water Cherenkov muon veto for the XENON1T experiment, J. Instrum. **9**, P11006 (2014).
[8] E. Aprile *et al.* (XENON Collaboration), Projected WIMP sensitivity of the XENONnT dark matter experiment, J. Cosmol. Astropart. Phys. 11 (2020) 031.
[9] A. Antochi *et al.*, Improved quality tests of R11410-21 photomultiplier tubes for the XENONnT experiment, J. Instrum. **16**, P08033 (2021).
[10] G. Plante, E. Aprile, J. Howlett, and Y. Zhang, Liquid-phase purification for multi-tonne xenon detectors, Eur. Phys. J. C **82**, 860 (2022).
[11] M. Murra, D. Schulte, C. Huhmann, and C. Weinheimer, Design, construction and commissioning of a high-flow radon removal system for XENONnT, Eur. Phys. J. C **82**, 1104 (2022).
[12] E. Aprile *et al.* (XENON Collaboration), Material radiopurity control in the XENONnT experiment, Eur. Phys. J. C **82**, 599 (2021).
[13] E. Aprile *et al.* (XENON Collaboration), Search for New Physics in Electronic Recoil Data from XENONnT, Phys. Rev. Lett. **129**, 161805 (2022).
[14] E. Aprile *et al.* (XENON Collaboration), The triggerless data acquisition system of the XENONnT experiment, arXiv:2212.11032 [J. Instrum. (to be published)].
[15] E. Aprile *et al.* (XENON Collaboration), The XENON1T data acquisition system, J. Instrum. **14**, P07016 (2019).
[16] J. Aalbers *et al.*, AxFoundation/strax (2022), 10.5281/zenodo.1340632.
[17] XENON Collaboration, XENONnT/straxen: Streaming analysis for XENON(nT), 10.5281/zenodo.5576262 (2022).
[18] E. Aprile *et al.* (XENON Collaboration), XENON1T dark matter data analysis: Signal reconstruction, calibration and event selection, Phys. Rev. D **100**, 052014 (2019).
[19] S. Liang, A. Higuera, C. Peters, V. Roy, W. U. Bajwa, H. Shatkay, and C. D. Tunnell, Domain-informed neural networks for interaction localization within astroparticle experiments, Front. Artif. Intell. **5**, 832909 (2022).
[20] XENON Collaboration, XENONNT/WFSIM: v1.0.2, 10.5281/zenodo.7216324 (2022).
[21] COMSOL AB, COMSOL MULTIPHYSICS, https://www.comsol.com.
[22] D. Akerib *et al.* (LUX Collaboration), $^{83\mathrm{m}}$Kr calibration of the 2013 LUX dark matter search, Phys. Rev. D **96**, 112009 (2017).
[23] G. Carugno, B. Dainese, F. Pietropaolo, and F. Ptohos, Electron lifetime detector for liquid argon, Nucl. Instrum. Methods Phys. Res., Sect. A **292**, 580 (1990).
[24] F. Jörg, D. Cichon, G. Eurin, L. Hötzsch, T. Marrodán Undagoitia, and N. Rupp, Characterization of alpha and beta interactions in liquid xenon, Eur. Phys. J. C **82**, 361 (2022).
[25] E. Aprile *et al.* (XENON Collaboration), Excess electronic recoil events in XENON1T, Phys. Rev. D **102**, 072004 (2020).
[26] C. E. Dahl, The physics of background discrimination in liquid xenon, and first results from XENON10 in the hunt for WIMP dark matter, Ph.D. thesis, Princeton University, 2009.
[27] J. Scherzinger, J. Annand, G. Davatz, K. Fissum, U. Gendotti, R. Hall-Wilton, E. Håkansson, R. Jebali, K. Kanaki, M. Lundin, B. Nilsson, A. Rosborge, and H. Svensson, Tagging fast neutrons from an ^{241}Am/^{9}Be source, Appl. Radiat. Isot. **98**, 74 (2015).
[28] S. Agostinelli *et al.* (GEANT4 Collaboration), GEANT4—a simulation toolkit, Nucl. Instrum. Methods Phys. Res., Sect. A **506**, 250 (2003).
[29] R. F. Lang, A. Brown, E. Brown, M. Cervantes, S. Macmullin, D. Masson, J. Schreiner, and H. Simgen, A Rn-220 source for the calibration of low-background experiments, J. Instrum. **11**, P04004 (2016).
[30] E. Aprile *et al.* (XENON Collaboration), Low-energy calibration of XENON1T with an internal ^{37}Ar source, Eur. Phys. J. C **83**, 542 (2023).
[31] E. Aprile *et al.* (XENON Collaboration), XENON1T dark matter data analysis: Signal and background models and statistical inference, Phys. Rev. D **99**, 112009 (2019).
[32] E. Aprile *et al.* (XENON Collaboration), Search for Coherent Elastic Scattering of Solar ^{8}B Neutrinos in the XENON1T Dark Matter Experiment, Phys. Rev. Lett. **126**, 091301 (2021).
[33] XENON Collaboration, XENONNT/PEMA, 10.5281/zenodo.7219740 (2022).
[34] See Supplemental Material at http://link.aps.org/supplemental/10.1103/PhysRevLett.131.041003 for details, which includes Refs. [35–37].
[35] E. Aprile *et al.* (XENON Collaboration), Constraining the Spin-Dependent WIMP-Nucleon Cross Sections with XENON1T, Phys. Rev. Lett. **122**, 141301 (2019).
[36] P. Klos, J. Menéndez, D. Gazit, and A. Schwenk, Large-scale nuclear structure calculations for spin-dependent WIMP scattering with chiral effective field theory currents, Phys. Rev. D **88**, 083516 (2013); **89**, 029901(E) (2014).
[37] M. Hoferichter, P. Klos, J. Menéndez, and A. Schwenk, Analysis strategies for general spin-independent WIMP-nucleus scattering, Phys. Rev. D **94**, 063505 (2016).
[38] XENON Collaboration, XENONnT/epix: Electron and photon instructions generator for XENON, 10.5281/zenodo.7516942 (2023).

[39] B. Aharmim *et al.* (SNO Collaboration), Combined analysis of all three phases of solar neutrino data from the Sudbury neutrino observatory, Phys. Rev. C **88**, 025501 (2013).

[40] D. Baxter *et al.*, Recommended conventions for reporting results from direct dark matter searches, Eur. Phys. J. C **81**, 907 (2021).

[41] J. D. Lewin and P. F. Smith, Review of mathematics, numerical factors, and corrections for dark matter experiments based on elastic nuclear recoil, Astropart. Phys. **6**, 87 (1996).

[42] J. Bland-Hawthorn and O. Gerhard, The galaxy in context: Structural, kinematic, and integrated properties, Annu. Rev. Astron. Astrophys. **54**, 529 (2016).

[43] R. Abuter *et al.* (GRAVITY Collaboration), Improved GRAVITY astrometric accuracy from modeling optical aberrations, Astron. Astrophys. **647**, A59 (2021).

[44] G. Cowan, K. Cranmer, E. Gross, and O. Vitells, Power-constrained limits, arXiv:1105.3166.

[45] L. Marti *et al.*, Evaluation of gadoliniums action on water Cherenkov detector systems with EGADS, Nucl. Instrum. Methods Phys. Res., Sect. A **959**, 163549 (2020).

[46] K. Abe *et al.* (Super-Kamiokande Collaboration), First gadolinium loading to Super-Kamiokande, Nucl. Instrum. Methods Phys. Res., Sect. A **1027**, 166248 (2022).